nature communications

Article

https://doi.org/10.1038/s41467-025-68078-5

Reduction of bacterial colonization on buckling-induced wrinkled surfaces under fluid shear

Received: 18 May 2025

Accepted: 16 December 2025

Published online: 07 January 2026

Check for updates

Luca Pellegrino[1,2] ✉, Giovanni Savorana[3], Valeria Cassina[4], Riccardo Campanile[4], Martin Centola[2,5], Cristina Belgiovine[6], Valeriano Vinci[1,2], Marco Klinger[2,7], Sigolène Lecuyer[8], Edoardo D'Imprima[2,5], Francesco Mantegazza[4], Eleonora Secchi[3] & Roberto Rusconi[1,2] ✉

Microbial colonization and biofilm formation drive infection persistence and the spread of antimicrobial resistance, particularly under flow conditions typical of medical and natural environments. Here, we combine spontaneously buckled wrinkled topographies with microfluidic platforms to investigate the adhesion of *Pseudomonas aeruginosa* and *Staphylococcus aureus* across shear rates of 0.4-200 s^{-1}. Wrinkled surfaces with tunable wavelengths (0.5-20 μm) are fabricated and characterized using optical, atomic force, and scanning electron microscopy. Sinusoidal wrinkles with a 2 μm wavelength reduce bacterial colonization by over 70% when oriented perpendicular to flow, while folded wrinkles of 5 μm achieve more than 90% reduction across broader shear regimes and suppress biofilm formation by over 85% relative to flat controls. These topographies retain antifouling performance under pulsatile flow. This work demonstrates a scalable, chemical-free strategy for passive biofilm control through geometric surface design, enabling durable antimicrobial materials for biomedical and industrial applications.

Material surface properties critically influence bacterial adhesion through direct physicochemical interactions—such as roughness and surface energy—as well as indirect interactions mediated by adsorbed molecules or preconditioning films[1,2]. Following irreversible attachment to a substrate, bacteria often develop matrix-encased colonies known as biofilms. Biofilms protect bacteria from immune responses and antibiotics, making them highly resilient and a leading cause of persistent infections[3].

The effects of nano and microscale surface topography on bacterial attachment and subsequent biofilm formation have been explored through various mechanisms[4–8]. Nanoscale features can modulate surface energy, cell membrane deformation, and interfacial chemical gradients, mimicking the bactericidal properties of natural nanopatterns found on cicada and dragonfly wings[9–11]. In contrast, microscale structures (above 1 µm) primarily affect surface hydrodynamics, microbial entrapment, and surface conditioning[2,12–14]. Topographies comparable in scale to bacterial dimensions (≈1–3 µm) can direct spatial organization and proliferation by modulating key parameters, such as periodicity, amplitude, and curvature. Specific geometries that reduce the available fouling area[15], limit adhesive contact points[16], or alter local curvature[17] can physically confine bacteria, restricting motility and intercellular connections[2,18,19] and thereby disrupting biofilm formation.

Natural biological tissues provide inspiration for such design strategies. Many interfaces—from cerebral cortices to skin and gut epithelia—exhibit wrinkled or folded morphologies arising from

[1]Department of Biomedical Sciences, Humanitas University, Pieve Emanuele, Italy. [2]IRCCS Humanitas Research Hospital, Rozzano, Italy. [3]Institute of Environmental Engineering, ETH Zürich, Zürich, Switzerland. [4]School of Medicine and Surgery, University of Milano-Bicocca, Vedano al Lambro, Italy. [5]Correlative Light and Electron Microscopy Core, Humanitas University, Pieve Emanuele, Italy. [6]Department of Biology and Biotechnology, University of Pavia, Pavia, Italy. [7]Department of Medical Biotechnologies and Translational Medicine, University of Milan, Milan, Italy. [8]Laboratoire de Physique (LPENSL UMR 5672), CNRS, ENS de Lyon, Lyon Cedex 07, France. ✉e-mail: luca.pellegrino@humanitasresearch.it; roberto.rusconi@hunimed.eu

mechanical instabilities in layered systems[20,21]. These topographies influence not only mechanical behavior but also biological interactions, shaping how cells, fluids, and microbes engage with surfaces. Reproducing and controlling these morphologies synthetically enables fundamental studies of bacterial adhesion and biofilm dynamics, as well as the design of functional surfaces for medical and industrial use[3]. Hydrodynamic conditions further complicate these interactions. In flowing environments, shear stress strongly affects bacterial attachment and colonization[22,23]. The interplay between fluid dynamics and surface topography is complex, as local flow rates and mechanical stresses are governed by the geometry and spatial arrangement of surface features[23,24]. Although previous studies have investigated bacterial responses to either surface topography or hydrodynamic shear independently, their combined and dynamic effects remain poorly understood.

In this work, we investigate the coupled influence of surface-induced mechanical confinement and shear-induced local stress variations on bacterial colonization. We engineer buckling-induced wrinkled and folded topographies with controlled geometries and integrate them into microfluidic channels. Using *Pseudomonas aeruginosa* (*P. aeruginosa)* and *Staphylococcus aureus* (*S. aureus*)—two clinically relevant pathogens associated with device-related infections—we demonstrate how wrinkling instabilities can be harnessed to mitigate bacterial adhesion and biofilm formation in biomedical and industrial contexts.

Results

Wrinkled patterns within microfluidic channels

Wrinkled patterns can be generated in multilayered structures subjected to mechanical deformation and plasma oxidation. Specifically, in a bilayer system consisting of a semi-infinite soft substrate of elastic modulus E_s and a thin, stiff top layer of elastic modulus E_f, spontaneous buckling instabilities arise under compression once a critical strain (ϵ_c) is exceeded. The resulting buckling regime depends on both the magnitude and direction of the applied strain (ϵ). For moderate strains (up to ~20%), a sinusoidal wrinkling mode emerges, characterized by a wavelength (λ) and amplitude (A) dictated by the mechanical mismatch between the bilayer components ("Methods"), with an aspect ratio of A/λ ranging from 0.1 to 0.2. At higher compressions (~40%), purely sinusoidal wrinkles transition into folds, ridges, creases, or even delaminated buckling, depending on the bending energy of the film, the viscoelastic properties of the substrate, and the interfacial energies[25]. Building upon prior studies of wrinkling mechanics[15,26–33], we engineered patterned surfaces with prescribed wavelengths and topographies, constructing a phase diagram of the explored wrinkling instabilities (Fig. 1a).

We focused on two distinct pattern modes: sinusoidal wrinkling (w_s) with periodicities (λ) of 0.5 and 2 μm, and doubling/folding (w_f) patterns with λ of 5 and 20 μm (Fig. 1a). These patterns were generated through plasma oxidation of silicone polymers[30,31]. The formation of sinusoidal wrinkled surfaces was controlled by adjusting the stiffness of the polydimethylsiloxane (PDMS) bilayer, while, to induce folding, a lower modulus mismatch between the bilayer components was required. This was accomplished using Ecoflex ($E_s \approx 100$ kPa) as the foundation material, which enabled a purely folding instability under 50% compressive strain[25,34]. Details of the fabrication process are provided in the "Methods" section. To preserve the mechanical properties of the bilayer materials and the integrity of the wrinkled patterns, we eliminated the glassy layer formed during PDMS and Ecoflex surface vitrification using a replication strategy. This involved

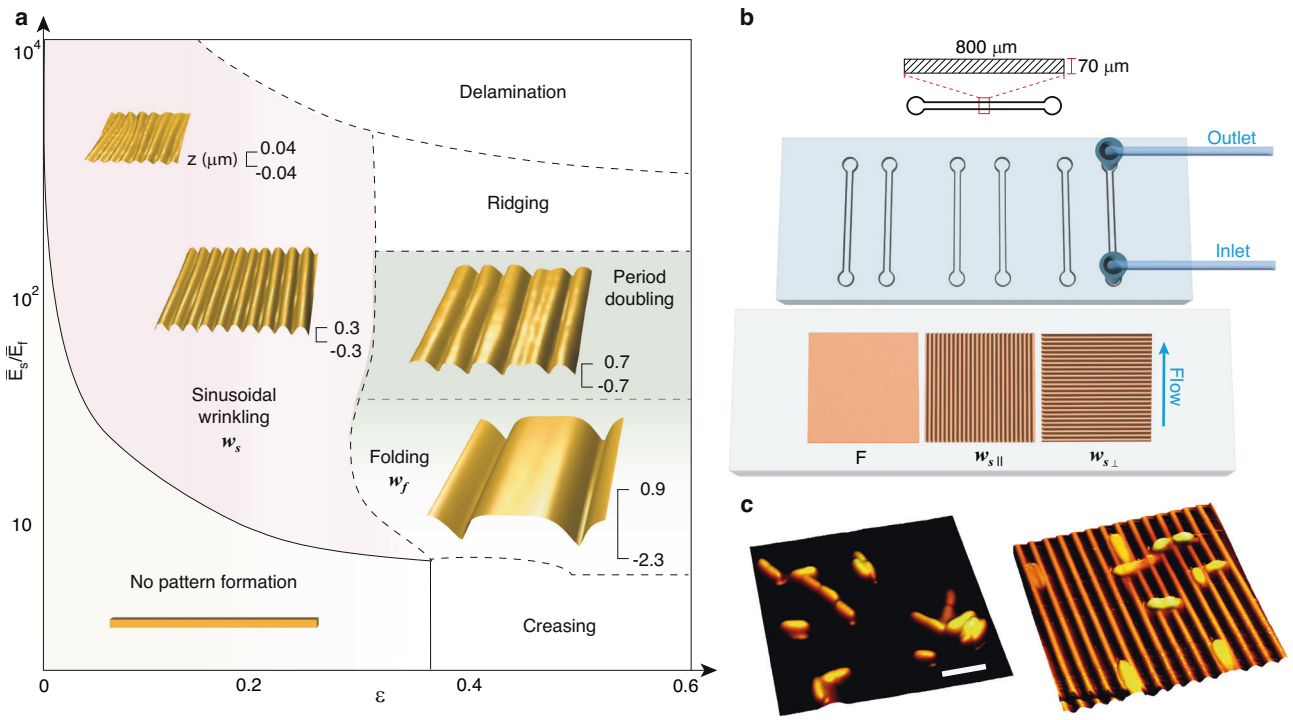

Fig. 1 | Tunable patterned surfaces are fabricated via spontaneous buckling and integrated into a microfluidic device. a Phase diagram illustrating the mechanical instability modes in soft bilayers, computing the mismatch in mechanical properties as the ratio of the elastic modulus of the foundation material E_s over the elastic modulus of the thin film layer E_f. Representative 3D atomic force microscopy (AFM) projections show experimental sinusoidal wrinkling (w_s) and period-doubling/folding modes (w_f) observed in our plasma-oxidized silicone elastomeric substrates. **b** Schematic of the microfluidic wrinkled device. The upper section consists of six straight polydimethylsiloxane (PDMS) channels, each with a cross-section of 70 × 800 μm (height × width). The lower section features a PDMS substrate with a flat (unpatterned, F) surface and two sinusoidal wrinkling patterns w_s: one aligned parallel to the flow direction ($w_{s\parallel}$) and one perpendicular to it ($w_{s\perp}$). **c** AFM images showing representative 3D projections of adhered *Pseudomonas aeruginosa* on a flat surface (F) and on a sinusoidal w_s pattern within the microfluidic wrinkling device. Scale bar, 5 μm.

silanization with octadecyltrichlorosilane (OTS), followed by PDMS molding. Because a single silanization-replication step inverts the surface topography, we performed a double replication to restore the original concavity. The first replica was gently plasma-oxidized, passivated in ethanol vapor to remove unreacted PDMS monomers, and then molded with fresh PDMS.

The w_s and w_f patterned surfaces were integrated into a custom-designed microfluidic device, hereafter referred to as the "microfluidic wrinkling" device (Fig. 1b). These patterned surfaces formed the bottom of a microfluidic channel with a rectangular cross-section of 800 × 70 µm (width × height) and oriented in two configurations, namely according to the flow direction ($w_{s\parallel}$, $w_{f\parallel}$) and perpendicular to the flow direction ($w_{s\perp}$, $w_{f\perp}$). Multiple channels were assembled on a microscope glass slide to enable direct visualization. We used this setup to investigate the colonization of wrinkled surfaces by pathogenic bacteria, employing phase-contrast and fluorescence imaging on an inverted microscope ("Methods") and atomic force microscopy (AFM) for high-resolution surface and bacteria characterization (Fig. 1c).

To investigate the impact of surface topography on fluid flow, we performed numerical simulations of rod-shaped bacteria attached to sinusoidal w_s and folding w_f surfaces ("Methods"). Wrinkled profiles significantly alter the local shear field, generating stress concentration points at the hilltops where the calculated shear rate is 2–3 times higher than that of a flat surface (Fig. 2a). When a bacterium settles in the valley regions, corresponding to the periodic minima of the sinusoid (Fig. 2b, left), the contact area is maximized while the experienced flow velocity and shear stress are minimized, creating favorable conditions for attachment. In contrast, a bacterium positioned at the hilltops, perpendicular to the pattern direction, has limited contact area, primarily at its poles (Fig. 2b, right), and experiences shear stress hotspots. Notably, these stress enhancements were more pronounced for sinusoidal patterns oriented perpendicular rather than parallel to the flow, as the fluid directly interacts with the polar region of the cell. On $w_{f\perp}$ surfaces with $\lambda = 5$ µm and $A/\lambda = 0.4$, the folding geometry further modifies the shear rate distribution, producing hotspots up to 4 times higher than on flat surfaces (Fig. 2c). For the same geometry but with larger wavelengths ($\lambda = 20$ µm) and lower aspect ratio ($A/\lambda = 0.2$), the pattern length scales exceed bacterial dimensions, creating larger low-shear regions (Fig. 2d). Comparing velocity streamlines for $w_{f\perp}$ surfaces with $A/\lambda = 0.4$ (Fig. 2e, left) and $w_{s\perp}$ surfaces with $A/\lambda = 0.25$ (Fig. 2e, right), recirculation zones were observed only for the former folding pattern.

Our simulations demonstrate that surface topography critically shapes local hydrodynamic conditions by redistributing shear stresses at the cell-fluid interface. On sinusoidal features, ridge crests concentrate shear due to curvature-induced flow acceleration, whereas valleys act as stagnation zones with reduced velocity gradients. This is consistent with prior theoretical studies showing that curvature generates stress concentration points and alters near-wall shear layers[35]. Folding geometries with $\lambda = 5$ µm and $A/\lambda = 0.4$ further amplify these effects: they not only elevate local shear by up to fourfold compared to flat surfaces but also induce localized recirculation zones. Such recirculation may act to further inhibit bacterial settlement[2,19], thereby reinforcing the antifouling potential of these topographies.

Effect of fluid shear on the attachment of *Pseudomonas aeruginosa* on wrinkled surfaces

Building on insights from our numerical simulations of bacterial attachment to patterned surfaces, we conducted experimental investigations using the microfluidic wrinkling device. A suspension of GFP-labeled *P. aeruginosa* PA14 cells ($OD_{600} = 0.2$) was introduced at an average shear rate of $\dot{\gamma} = 80\ s^{-1}$, a value comparable to that encountered in catheters and stents[3,22]. The surfaces under study included a flat control (F), $w_{s\parallel}$, and $w_{s\perp}$, with a wavelength of 2 µm. Fluorescence and phase-contrast imaging (Supplementary Information, Fig. S1) were used to analyze the behavior of PA14 on these surfaces over a 4-h period. On flat surfaces, *P. aeruginosa* formed individual colonies that expanded and proliferated randomly across the surface. In contrast, bacterial colonization was reduced on both $w_{s\parallel}$ and $w_{s\perp}$ surfaces.

We then examined bacterial surface coverage on the sinusoidal 2 µm wrinkled surface across a range of shear rates (0.4–200 s^{-1}) that mimic physiological conditions[3,22,36]. To quantify bacterial colonization within the first 4 h of exposure to flowing bacterial suspensions, we calculated the surface coverage (S_c), defined as the percentage of surface area covered by bacterial cells, as well as the normalized surface coverage (S_c/S_F), where S_F denotes the coverage on flat control surfaces at the corresponding time point. Our analysis revealed that the normalized surface coverage on both $w_{s\parallel}$ and $w_{s\perp}$ surfaces decreased with increasing shear rates (Fig. 3a, b).

To assess the effect of flow direction relative to the surface pattern, we analyzed bacterial orientation on F, $w_{s\parallel}$, and $w_{s\perp}$ surfaces at the 2-h mark using a computed probability distribution function (PDF) (Fig. 3c). Fluorescence images were segmented into discrete sections, and fast Fourier transform (FFT) techniques were applied to determine bacterial orientation relative to both the wrinkles and the imposed flow direction. By combining individual FFTs, we obtained an overall PDF, which provided insights into the angular distribution of PA14 cells. On flat surfaces, the PDF spanned the full angular range, with a slight polarization at zero radians, indicating weak alignment along the flow direction due to fluid shear, an effect already observed for microscale, elongated particles[37]. In contrast, surface patterning significantly affected orientation. On $w_{s\parallel}$ surfaces, bacteria exhibited a pronounced alignment where flow and pattern direction were parallel. On $w_{s\perp}$ surfaces, where wrinkles opposed the flow, bacterial orientation was evenly distributed between the pattern direction ($\pm\pi/2$ radians) and the flow direction (zero radians). These effects were evident in the FFT insets of Fig. 3c, which showed an isotropic circular distribution on flat surfaces (top), an elongated ellipse aligned with both flow and pattern directions on $w_{s\parallel}$ (center), and a cross-shaped distribution resulting from the competing influences of flow and surface patterning on $w_{s\perp}$ (bottom). Furthermore, AFM imaging revealed distinct bacterial organization across the different surfaces (Supplementary Information, Fig. S2). After the experiment, the microfluidic winkling chip was filled with 4% paraformaldehyde (PFA) to fix bacterial cells before being opened for AFM imaging. The measured bacterial cell length of 2.5–3 µm on the F control was consistent with existing literature[15]. However, on wrinkled surfaces, PA14 cells preferentially settled in pattern valleys, where their length was reduced to ~2 µm, likely due to physical constraints[15].

Analyzing the surface coverage S_c on both w_s surfaces compared to a flat surface at the 3-h time point, we observed three distinct regimes in response to varying shear rates (Fig. 3d). At low shear rates (0.4 s^{-1}), wrinkled surfaces exhibited slightly higher bacterial coverage than flat surfaces, a phenomenon we termed low-shear adhesion. In this regime, bacteria tend to occupy the entire available surface without hindrance from shear forces. The orientation of the pattern has minimal influence on colonization, as motile PA14 cells can adhere to both $w_{s\parallel}$ and $w_{s\perp}$ surfaces without significant differences. However, at shear rates exceeding ~1 s^{-1}, a transition occurs. Flat surfaces exhibited increased bacterial coverage with rising shear rates, consistent with prior reports showing that motile bacteria become trapped in high-shear regions of Poiseuille flow, which enhances encounter frequency and promotes surface colonization[22]. In contrast, on both $w_{s\parallel}$ and $w_{s\perp}$ wrinkled surfaces, bacterial coverage decreased as shear rate increased. This shear-decreased adhesion behavior occurs because, despite the modest increase in surface area (~10%, "Methods") and the near-wall accumulation driven by shear trapping, bacterial colonization is confined primarily to the low-shear valleys of the sinusoidal pattern. These valleys represent approximately 60–70% of

https://doi.org/10.1038/s41467-025-68078-5

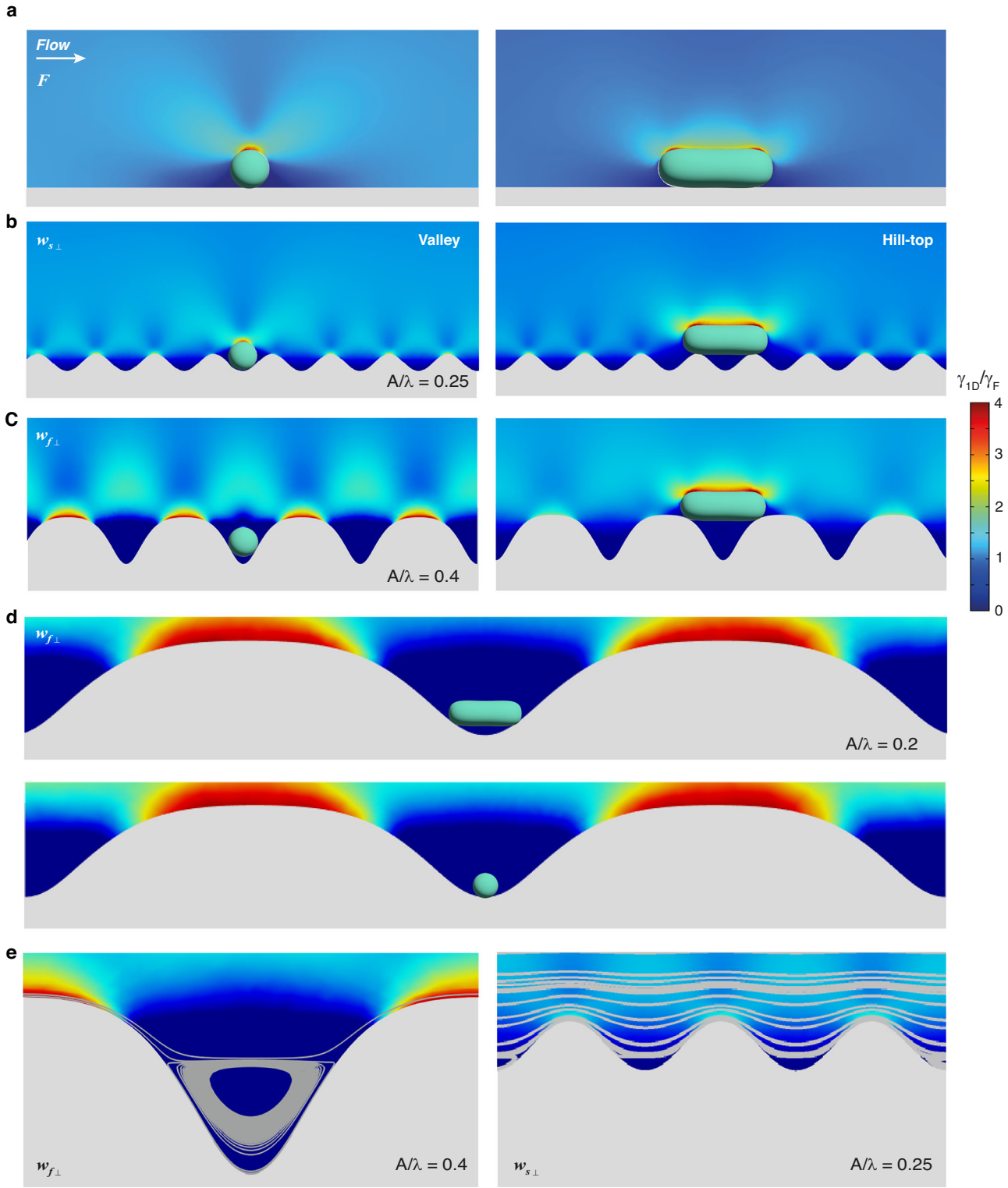

Fig. 2 | Numerical simulations reveal how wrinkled topographies and attached bacteria generate shear gradients that influence surface colonization. a Rod-shaped bacterium attached to a flat surface (F), with orientation perpendicular (left) and parallel (right) to the flow, under a defined shear rate of $\dot{\gamma} = 80\,s^{-1}$. **b** Sinusoidal wrinkled surface $\lambda = 2\,\mu m$ and $A/\lambda = 0.25$, oriented perpendicularly to the flow direction ($w_{s\perp}$). **c** Folding surface with $\lambda = 5\,\mu m$ and $A/\lambda = 0.4$, oriented perpendicularly to the flow direction ($w_{f\perp}$). **d** Folding surface with $\lambda = 20\,\mu m$ and $A/\lambda = 0.2$, oriented perpendicularly to the flow direction ($w_{f\perp}$). Two attachment configurations were considered: hilltop attachment and valley attachment. Bacteria were modeled as cylinders with hemispherical caps (radius $R = 0.5\,\mu m$, total length $L = 3\,\mu m$). **e** Flow streamlines for a $w_{f\perp}$ surface ($A/\lambda = 0.4$), showing the occurrence of recirculation zones in the valley region (left), and for a $w_{s\perp}$ surface ($A/\lambda = 0.25$, right). Data are reported as normalized "excess shear rate" ($\dot{\gamma}_{w_s}/\dot{\gamma}_F$).

https://doi.org/10.1038/s41467-025-68078-5

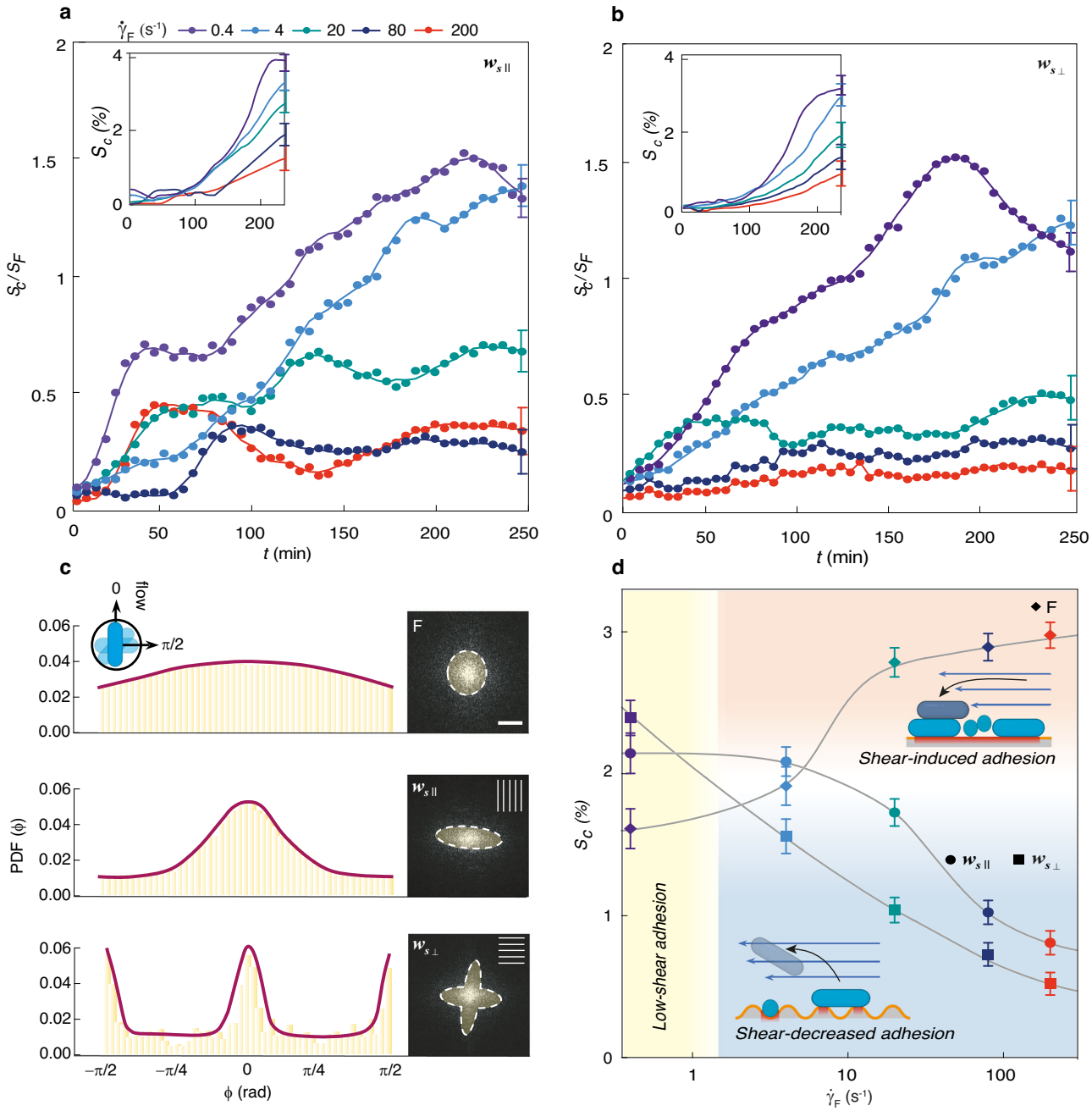

Fig. 3 | Shear flow and pattern orientation modulate *Pseudomonas aeruginosa* PA14 adhesion on wrinkled surfaces. Temporal evolution of the surface coverage S_c (insets) of wild-type *P. aeruginosa* PA14 on 2 µm wrinkled surfaces, $w_{s\parallel}$ (**a**) and $w_{s\perp}$ (**b**), normalized by the coverage of a flat (F) surface (S_c/S_F) across different shear rates. **c** Probability distribution functions of bacterial orientation obtained from the fluorescent images shown in Fig. S1a for the F, $ws_{\parallel}$, and $ws_{\perp}$ after 2 h of continuous flow. Insets display the fast Fourier transform of the distribution. Scale bar is 0.02 µm^{-1}. Created in BioRender. Rusconi, R. (2025) https://BioRender.com/ihbaq87. **d** Comparison of surface coverage on $w_{s\parallel}$ (circle) and $w_{s\perp}$ patterns (squares) at different shear rates with a flat surface (diamonds) at the 3-h time point. Insets represent schematic representations of the shear-induced adhesion phenomenon observed on flat surfaces and the shear-decreased adhesion behavior observed on wrinkled substrates. Created in BioRender. Rusconi, R. (2025) https://BioRender.com/7g5edk6. For **a**, **b**, **d**, data represent the mean ± SEM from at least $N = 500$ cells per frame, three frames per channel, and three technical channels per condition, with three independent biological replicates. Source data are provided as a Source data file.

the total surface area relative to an equivalent flat substrate, owing to their slightly broader and deeper geometry compared to the ridge crests. This estimate was obtained from line-integral analysis of the sinusoidal profile and validated by AFM cross-sectional imaging[15]. In contrast, adhesion at the peaks is reduced by elevated local wall shear stress and by limited effective contact with the surface. Consequently, motile bacteria must reorient through tumbling or twitching to achieve stable attachment; failure to do so leads to detachment by fluid flow, an effect that becomes more pronounced at higher shear rates. Detachment is further amplified on $w_{s\perp}$ surfaces, where the misalignment between flow direction and surface pattern enhances removal, as schematically shown in Fig. 3d. Together, these findings demonstrate that the interplay between surface topography and shear forces critically shapes bacterial adhesion, with wrinkled surfaces selectively suppressing colonization under elevated shear rates.

https://doi.org/10.1038/s41467-025-68078-5

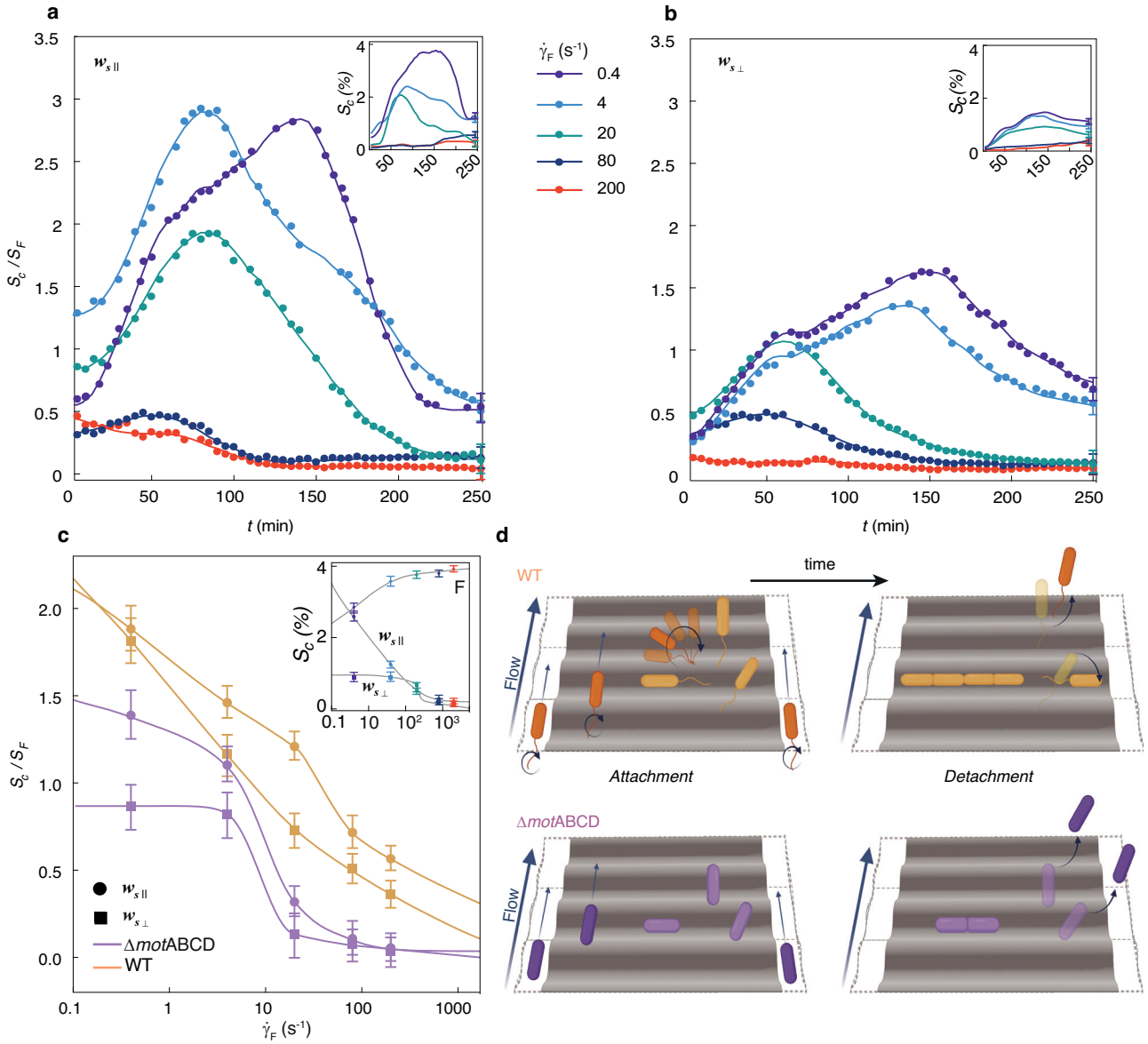

Fig. 4 | Motility influences the adhesion response of *Pseudomonas aeruginosa* to shear on wrinkled surfaces. a, **b** Normalized surface coverage (S_c/S_F) of the non-motile PA14 *ΔmotABCD* on $w_{s\parallel}$ (left) and $w_{s\perp}$ (right) surfaces at different time points and shear rates. **c** Normalized surface coverage (S_c/S_F) as a function of shear rate, comparing the PA14 Δ*motABCD* mutant and wild-type (WT) PA14 on on $w_{s\parallel}$ (circles) and $w_{s\perp}$ (squares) surfaces. **d** Schematic depicting the attachment and detachment behavior of WT (orange) and Δ*motABCD* mutant (purple) strains on $w_{s\perp}$ surfaces. Created in BioRender. Rusconi, R. (2025) https://BioRender.com/2ckm3h6. For **a**–**c**, data represent the mean ± SEM from at least $N = 500$ cells per frame, three frames per channel, and three technical channels per condition, with three independent biological replicates. Source data are provided as a Source data file.

Impact of surface wrinkling on the attachment of non-motile *Pseudomonas aeruginosa* mutants

To examine the role of motility in bacterial surface coverage on wrinkled surfaces, we compared the behavior of the wild-type PA14 strain with a non-motile mutant lacking the flagellar motor, PA14 Δ*motABCD* (Fig. 4a, b). The shear-induced adhesion on the flat substrate observed for the wild-type strain was notably less pronounced in the mutant (Fig. 4c and Supplementary Information, Fig. S3), consistent with expectations for non-motile microswimmers[22]. Unlike the wild-type strain, the mutant initially exhibited an increase in surface coverage on both wrinkled surfaces, followed by a gradual decline, indicating detachment across all tested shear rates. The transition point from attachment to detachment varied with shear rate, occurring earlier at higher shear rates. Analyzing the normalized surface coverage relative to an equivalent flat surface (S_c/S_F) as a function of shear rate for both strains and surface types revealed a significant reduction in coverage for the mutant, particularly on $w_\perp$ surfaces (Fig. 4c).

Similar to passive particles, non-motile bacteria attach to surfaces only when their transporting streamline brings them into sufficient contact. Moreover, their attachment is weaker than that observed in wild-type strains, leading to shear-induced detachment at earlier time points. When bacteria encounter an unfavorable orientation relative to the surface pattern, motility allows them to reposition and achieve more favorable attachment conditions to resist fluid shear. However, the non-motile PA14 Δ*motABCD* strain lacks this ability, causing bacterial cells to behave as passive rods[37]. As a result, attachment under these conditions depends on the frequency of successful positioning events, and the absence of repositioning, combined with early detachment in high shear environments, explains the lower coverage

observed on both $w_{s\parallel}$ and $w_{s\perp}$ surfaces. This underscores the critical role of bacterial motility in adapting to dynamic environments, directly influencing attachment outcomes under mechanical constraints and fluid shear forces.

Influence of buckling regimes on *Pseudomonas aeruginosa* surface colonization

The colonization of *P. aeruginosa* on wrinkled surfaces is dictated by the interplay between surface topography and fluid flow. As shown in Fig. 1a, different pattern morphologies arise depending on the mechanical strain applied to the bilayer during fabrication. Specifically, w_s surfaces exhibit sinusoidal wrinkling, while w_f surfaces fall within the transitional regime between period doubling and folding. By definition, sinusoidal wrinkles are symmetric, with equal hilltop and valley areas. In contrast, folding patterns introduce asymmetry, with increased amplitude resulting from the progressive contact and merging of adjacent wrinkles. This post-buckling evolution transforms sinusoidal wrinkles into a new morphology characterized by deeper and narrower valleys, producing high-aspect-ratio structures. The formation of folds in Ecoflex bilayers results in larger wavelengths under identical plasma oxidation conditions compared to PDMS due to the lower modulus mismatch. In contrast, PDMS-plasma bilayers exhibit sinusoidal wrinkling because the higher modulus mismatch makes folding less energetically favorable. To quantify these morphological differences, we analyzed the curvature of the patterns using linear integration of 1D profiles extracted from AFM measurements (Supplementary information, Fig. S4). Symmetric sinusoidal patterns exhibit comparable minimum (κ_{min}) and maximum (κ_{max}) curvature values, whereas folding leads to steeper inflection points, deeper valleys, and an overall increase in pattern amplitude. We hypothesized that the reduced accessible valley areas in folding patterns could constrain bacterial attachment to hilltop regions, where cells were more exposed to fluid shear and, as a result, more susceptible to detachment.

We performed microfluidic experiments on wrinkled surfaces with wavelengths of 5 and 20 µm, as well as on smaller sinusoidal patterns with a wavelength of 0.5 µm, to assess their effect on microbial colonization. Our results showed that the 5 µm pattern led to a further reduction in surface colonization—up to 99% compared to a flat surface (Supplementary Table 1)—relative to the 2 µm pattern at a shear rate of 80 s^{-1}. In contrast, higher surface coverage was observed on 0.5 and 20 µm patterns (Fig. 5a, b). Moreover, surface coverage data plotted as a function of the pattern aspect ratio (A/λ) display that surfaces with aspect ratios greater than 0.25 effectively delayed colonization (Fig. 5c). Pattern aspect ratios were quantified using cross-sectional scanning electron microscopy (SEM) images obtained through focused ion beam (FIB) milling (Fig. 5d and Supplementary Information, Fig. S5). The folding pattern with $\lambda = 5$ µm and an aspect ratio of 0.4 proved to be the most effective geometry in limiting bacterial colonization.

Our findings are summarized schematically in Fig. 5e, where 1D cross-sectional profiles were extracted from AFM analysis. On 0.5 µm w_s surfaces, the measured $A/\lambda = 0.05$ was insufficient to significantly influence bacterial adhesion. A similar trend was observed for shallower 20 µm folding patterns ($A/\lambda = 0.2$), where extensive "flat-like" hilltop regions provided sufficient surface area for bacterial colonization. Although 2 µm w_s surfaces also effectively reduced PA14 coverage, the 5 µm w_f pattern emerged as the optimal compromise, combining a higher aspect ratio that effectively confined PA14 cells with an enhanced capacity for their removal by fluid flow. This effect was evident not only at 80 s^{-1}, consistent with the simulations shown in Fig. 2, but also across a broader range of shear rates (4–200 s^{-1}), as detailed in Supplementary Information (Fig. S6). For this pattern, orientation perpendicular to the flow direction further impaired surface coverage, including at lower flow rates and earlier colonization times. Overall, these results are consistent with our numerical simulations, which demonstrated that the combination of elevated shear at ridge crests and localized recirculation zones in valleys establishes hydrodynamic conditions that are unfavorable for stable bacterial attachment.

Role of buckling-induced surfaces in *Pseudomonas aeruginosa* colonization by type IV pili mutants

From our observations, the combination of sinusoidal ($w_{s\perp}$) and folding ($w_{f\perp}$) patterns with $0.25 < A/\lambda < 0.4$, together with fluid shear, was highly effective in reducing wild-type PA14 colonization. *P. aeruginosa* is well known to rely on type IV pili (T4P) for adhesion, surface sensing, twitching motility, and biofilm initiation[38–41]. Understanding the role of T4P in surface colonization is therefore critical for explaining how surface topography and fluid shear shape bacterial attachment. While the effect of shear stress on pili-depleted PA14 on glass and flat surfaces has been previously investigated[42], we sought to build on these findings by examining the contribution of surface topography and pili-dependent adhesion mechanisms. To this end, we tested our $w_{s\perp}$ and $w_{f\perp}$ patterns using the PA14 Δ*pilB* mutant.

The *pilB* gene encodes the extension ATPase required for producing dynamic type IV pili, which mediate initial attachment, mechanical sensing, and twitching motility. These functions promote bacterial accumulation in sheltered microenvironments and trigger downstream signaling pathways (e.g., cAMP and c-di-GMP) that drive biofilm initiation. In our experiments (Fig. 6a, b), PA14Δ*pilB* exhibited the same qualitative response to increasing shear and surface topography as the wild-type strain: surface coverage decreased with increasing shear, and surfaces with $A/\lambda = 0.4$ (5 µm folding wavelength) strongly limited colonization (Fig. 6c). However, compared with the wild-type, the Δ*pilB* strain consistently displayed lower coverage values across all conditions, indicating that T4P-mediated adhesion enhances the ability of *P. aeruginosa* to exploit low-shear valleys and resist detachment at high-shear ridges. This underscores the critical role of T4P in mediating the combined effects of surface topography and fluid shear on bacterial colonization.

Reduction of *Staphylococcus aureus* surface colonization on wrinkled substrates

To evaluate the potential of buckling-induced wrinkled substrates in reducing bacterial colonization across different bacterial species, we tested their effect on *S. aureus*, a Gram-positive pathogen, under fluid flow conditions. In contrast to *P. aeruginosa* PA14, a Gram-negative, motile, and ellipsoidal bacterium, *S. aureus* is non-motile, spheroidal, and typically measures between 1 and 1.5 µm in diameter. We selected the GFP-labeled *S. aureus* Newman strain[43], a clinically relevant human pathogen associated with strong virulence[44] and frequently implicated in nosocomial infections[45], bacteremia[46], endocarditis[47], and sepsis[48]. Furthermore, *S. aureus*, along with other Staphylococcus species, is a major contributor to periprosthetic joint infections, often leading to sepsis and implant failure in acute cases[49].

We first examined the effect of shear rate on 5 µm w_f surfaces (Fig. 7a) to assess whether the previously observed reduction in bacterial colonization also applied to *S. aureus*. Surface coverage analysis (Fig. 7b) confirmed that the shear-induced reduction in adhesion by the patterned surfaces persisted for this pathogenic strain, despite *S. aureus* displaying a higher overall surface coverage percentage (S_c(%)) compared to *P. aeruginosa* PA14. Notably, while *S. aureus* exhibited stronger adhesion, the reduction in colonization on wrinkled surfaces remained substantial (close to 90%, Supplementary Table 1). To further investigate the impact of surface geometry, we evaluated bacterial attachment across the four different w_s and w_f surface wavelengths and analyzed coverage as a function of the pattern aspect ratio (Fig. 7c, d). Again, patterns with wavelengths of 2 µm and, more effectively, 5 µm significantly reduced bacterial colonization, supporting the idea

https://doi.org/10.1038/s41467-025-68078-5

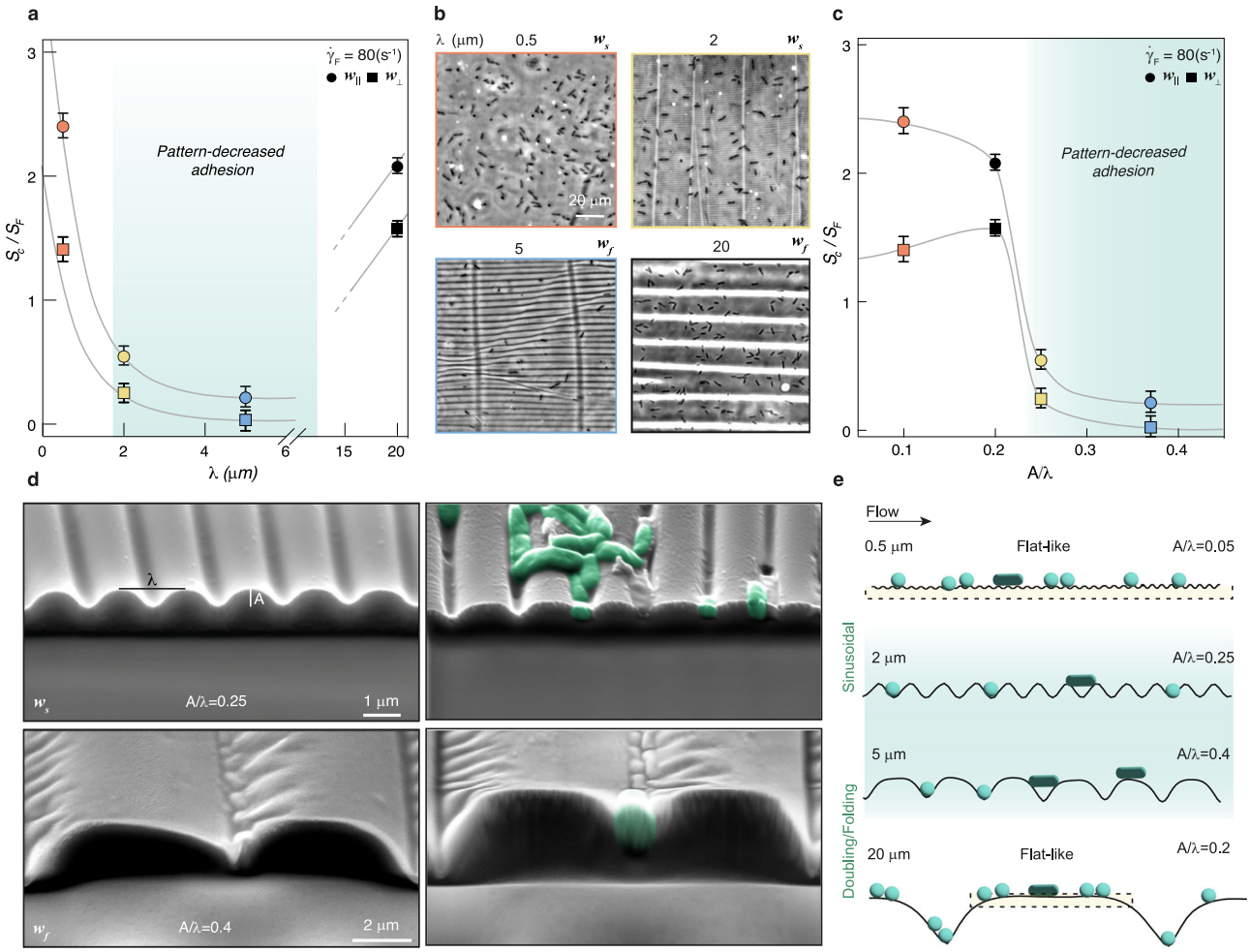

Fig. 5 | Surface wavelength and aspect ratio determine *Pseudomonas aeruginosa* PA14 adhesion on wrinkled and folded surfaces. a Normalized surface coverage (S_c/S_f) of *P. aeruginosa* PA14 cells, relative to an equivalent flat surface, at a shear rate of 80 s^{-1}. For $w_{s\parallel}$, $w_{f\parallel}$ (circles), $w_{s\perp}$, and $w_{f\perp}$ surfaces (squares), bacterial coverage decreases as λ increases up to 5 μm, followed by an increase at $\lambda = 20$ μm. **b** Phase-contrast microscopy images showing the attachment of PA14 wild-type cells on $w_{s\perp}$ and $w_{f\perp}$ surfaces with λ values of 0.5, 2, 5, and 20 μm at a shear rate of 80 s^{-1}. **c** Normalized surface coverage (S_c/S_f) of PA14 cells, relative to an equivalent flat surface, at a shear rate of 80 s^{-1}. Coverage is plotted for $w_{s\parallel}$, $w_{f\parallel}$ (circles), $w_{s\perp}$, and $w_{f\perp}$ surfaces (squares) as a function of pattern aspect ratio (A/λ). For surfaces with aspect ratios above 0.25, including 2 μm w_s and 5 μm w_f patterns, a decrease in bacterial adhesion is observed. **d** Scanning electron microscopy (SEM) images of 2 μm w_s and 5 μm w_f surfaces. Focused ion beam (FIB) milling cuts show surface cross-sectional profiles without PA14 cells (left) and with adhered PA14 cells (right). **e** Schematic representation of PA14 cells adhered to sinusoidal and folding profiles based on AFM measurements. Significant decreased adhesion is observed for patterns with A/λ values above 0.25. For **a**, data represent the mean ± SEM from at least $N = 500$ cells per frame, three frames per channel, and three technical channels per condition, with three independent biological replicates. Source data are provided as a Source data file.

of a synergistic pattern-decreased adhesion mechanism, further illustrated by the optical microscopy images (Fig. 7e). As observed with PA14 strains, these patterns hinder the establishment of stable adhesion sites. In contrast, the spherical morphology of *S. aureus* made adhesion insensitive to pattern orientation relative to fluid flow, as confirmed by the surface coverage data (Fig. 7b–d).

Effect of pulsatile flow on bacterial colonization on flat and wrinkled surfaces

To further analyze how patterned surfaces influence the attachment and removal of *P. aeruginosa* and *S. aureus* under physiologically relevant conditions, we performed additional experiments using a pulsatile flow regime representative of catheter and stent environments. Specifically, we tested $w_{f\perp}$ folding surfaces with $\lambda = 5$ μm. The syringe pump was programmed to alternate between $Q_{min} = 0$ μl/min and $Q_{max} = 4$ μl/min with a cycle period of $T = 10$ s, corresponding to a frequency of 0.1 Hz, which aligns with the bandwidth recommended for urodynamic measurements to capture physiological variations in urine flow[50]. The experiments were run for 900 cycles (2.5 h), yielding an average flow rate of $\bar{Q} = 2\,\mu$l/min, corresponding to an average shear rate of $\bar{\dot{\gamma}} = 80\ s^{-1}$ (Fig. 8a).

From the analysis of segmented microscopy images (Fig. 8b), we observed that both *S. aureus* and *P. aeruginosa* cells preferentially accumulated during the static phase (Q_{min}). Upon transition to peak flow (Q_{max}), exposure to shear rates of approximately $\dot{\gamma}_{max} = 160\ s^{-1}$ induced rapid detachment events, a pattern consistently observed across successive pulsatile cycles (Fig. 8b). Overall, pulsatile flow on wrinkled surfaces led to an even stronger reduction in surface colonization than continuous-flow conditions at the same mean shear rate, and to significantly lower colonization than flat surfaces under pulsatile flow (Fig. 8c, d). These dynamics resemble a "fill-and-flush" mechanism, where transient colonization occurs during quiescent intervals but is efficiently cleared during high-shear phases, with the folded surface geometry significantly amplifying this effect. Together, these findings highlight an additional dimension in the interplay between hydrodynamics and surface topography and further support the potential of wrinkled surfaces to mitigate colonization under conditions that more closely mimic those in medical devices.

https://doi.org/10.1038/s41467-025-68078-5

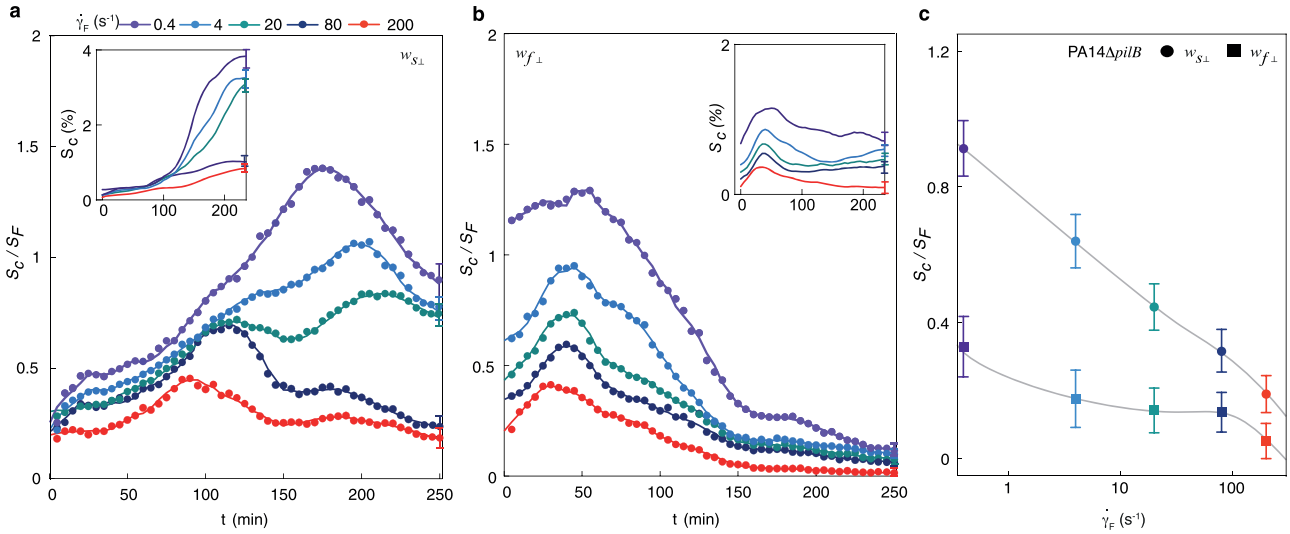

Fig. 6 | Wrinkled and folded substrates reduce surface colonization of type IV pili-defective *Pseudomonas aeruginosa* PA14 under shear flow. Normalized surface coverage (S_c/S_F) of PA14 Δ*pilB* on sinusoidal $w_{s\perp}$ (**a**, left) and folding $w_{f\perp}$ (**b**, right) surfaces at different time points and shear rates. **c** Normalized surface coverage (S_c/S_F) at 3 h as a function of shear rate for $w_{s\perp}$ (circles) and $w_{f\perp}$ (squares) surfaces. For **a**–**c**, data represent the mean ± SEM from at least $N = 500$ cells per frame, three frames per channel, and three technical channels per condition, with three independent biological replicates. Source data are provided as a Source data file.

Effect of pattern morphology and shear rate on biofilm formation

Our results demonstrate that w_s and w_f surface patterns in microfluidic wrinkling significantly reduce early-stage bacterial colonization for up to 4 h under a wide range of fluid flow and shear conditions. To further assess the potential application of these surfaces in biomedical devices, we performed a 24-h biofilm formation experiment comparing 5 µm w_f patterns, oriented perpendicular to the flow direction, to flat surfaces (Fig. 9). Propidium Iodide (PI), added at a final concentration of 1 µg/mL, was used to detect extracellular DNA associated with biofilm formation[51,52]. A shear rate of 200 s^{-1}, representative of conditions found in urinary catheters[3], was applied during the experiment. We used a bacterial suspension with an optical density (OD) of 0.005, which corresponds to approximately 10^5 cells/mL, a relatively high concentration that represents an evident state of bacterial contamination and is relevant for clinical applications. On flat surfaces (F), PA14 WT formed large colonies at 12 h, which continued to expand through 24 h (Fig. 9a). In contrast, *S. aureus* Newman formed bigger colonies at 12 h, highlighted by the strong binding of PI, eventually covering the entire surface by 24 h (Fig. 9b). On $w_\perp$ surfaces, no biofilm formation was observed for PA14 WT, although colonies did form by 24 h. For *S. aureus*, the valley regions of the $w_\perp$ surfaces were occupied, but full colony formation was not observed. These results highlight a significant reduction—i.e., more than 80% for both strains after 24 h (Supplementary Table 2)—in biofilm formation, demonstrating the potential of wrinkled surface patterns in reducing bacterial colonization in medical device applications, even under a high level of bacterial contamination.

Discussion

Our study demonstrates that microfluidic wrinkled surface patterns with wavelengths of 2–5 µm, generated through buckling instabilities, significantly reduce bacterial adhesion and biofilm formation under flow conditions. By evaluating *P. aeruginosa* and *S. aureus*, we found that these patterns effectively hinder bacterial colonization, even at high initial concentrations representative of clinical contamination. The reduction in surface coverage exceeded 90% under shear flow, underscoring the strong anti-adhesive properties of these substrates.

Biomedical devices and implants, particularly those subjected to fluid flow, such as urinary catheters and biliary stents, are highly susceptible to deterioration and fouling due to microbial colonization[3,23,53]. Catheters, which are widely used in hospitals for minimally invasive procedures—including urinary retention relief, blood sampling, nutrient transport, and dialysis—pose a significant risk of local or systemic infections as a result of bacterial attachment and biofilm formation[54,55]. Conventional approaches to prevent device-related infections primarily rely on periodic antibiotic flushing or the locking technique, in which an antibiotic solution is retained within the device for a specified duration[56]. However, the widespread use of antibiotics in such settings has contributed to the emergence of multidrug-resistant strains, limiting the effectiveness of these strategies[57]. In contrast, the implementation of wrinkled surface patterns offers an antibiotic-free approach to reduce bacterial colonization.

Our findings suggest that these microstructured surfaces can be seamlessly integrated into medical devices to significantly mitigate bacterial adhesion. These patterns could be generated through the buckling of laminated silicone tubes or replicated from 3D-printed negative masters, making them a scalable and cost-effective solution. By reducing initial bacterial attachment and biofilm formation, these surface modifications have the potential to extend device longevity, lower infection rates, and ultimately decrease the clinical reliance on antibiotics, thus addressing both medical and antimicrobial resistance challenges. Importantly, our results are most relevant to small-scale devices, such as catheters and stents, where flow remains laminar but shear rates can still be significant due to the narrow radii of the conduits. Under these conditions, antifouling behavior emerges only when surface pattern dimensions are comparable to bacterial size, whereas larger wavelengths (e.g., 20 µm) lose this effect and instead promote colonization (Supplementary Information, Fig. S7). This distinction highlights the difference from shark riblet structures, which rely on larger scales, complex denticle geometries, and vortex dynamics in turbulent regimes to achieve antifouling performance[58].

To investigate the coupling between fluid flow and surface topography in bacterial colonization, we leveraged microfluidic technology. The integration of multiple patterned surfaces within a single microfluidic chip was crucial for enabling direct, side-by-side

https://doi.org/10.1038/s41467-025-68078-5

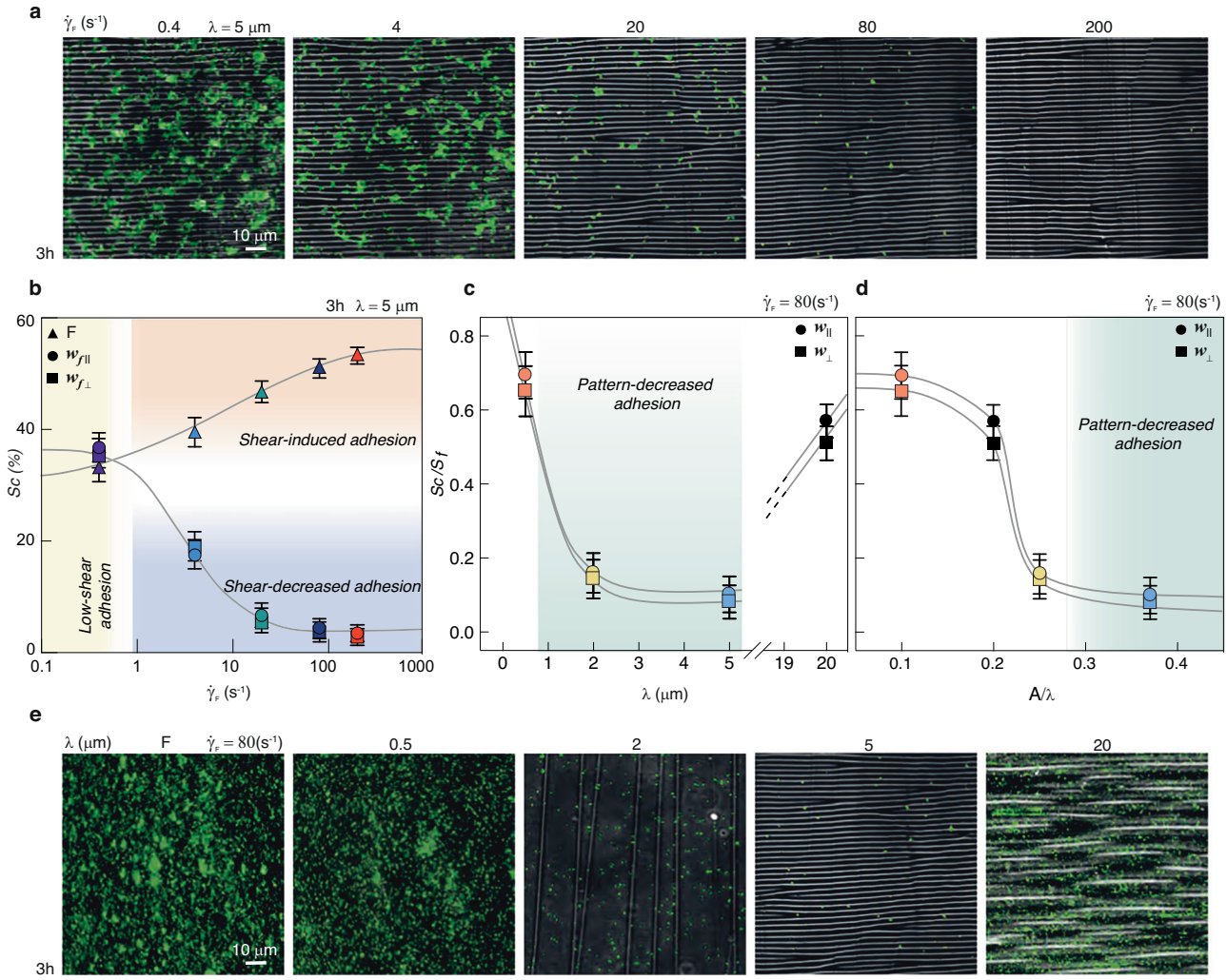

Fig. 7 | Shear flow and pattern geometry regulate *Staphylococcus aureus* surface colonization on folded substrates. a Fluorescence and phase-contrast overlaid optical microscopy images of *Staphylococcus aureus* Newman on 5 μm patterned $w_{f\perp}$ surfaces at different shear rates. **b** *S. aureus* Newman surface coverage (S_c) as a function of imposed shear stress on 5 μm patterned surfaces, comparing $w_{f\perp}$ (squares) and $w_{f\parallel}$ (circles) orientations with F surfaces (triangles) at 3 h. **c** *S. aureus* Newman normalized surface coverage (S_c/S_F) as a function of pattern wavelength at 3 h and a shear rate of 80 s^{-1} for parallel $w_\parallel$ (circles) and perpendicular $w_\perp$ orientations (squares). **d** *S. aureus* Newman normalized surface coverage (S_c/S_F) as a function of pattern aspect ratio (A/λ) at 3 h and a shear rate of 80 s^{-1} for parallel $w_\parallel$ (circles) and perpendicular $w_\perp$ orientations (squares). **e** Fluorescence and phase-contrast overlaid optical microscopy images of *S. aureus* Newman on $w_{f\perp}$ surfaces with different pattern wavelengths at 3 h. For **b**–**d**, data represent the mean ± SEM from at least $N = 500$ cells per frame, three frames per channel, and three technical channels per condition, with three independent biological replicates. Source data are provided as a Source data file.

comparisons under identical experimental conditions. This approach ensured that bacterial attachment and biofilm formation were evaluated simultaneously on different surfaces, using the same bacterial suspension and controlled ambient parameters, eliminating variations that could arise from batch-to-batch differences[22]. Beyond its biomedical relevance, fluid flow is a defining feature of microbial habitats, influencing colonization dynamics across a wide range of natural and artificial settings. The ability to control bacterial adhesion and biofilm formation through surface engineering has potential benefits in industries such as food processing, water filtration, and marine engineering. For instance, mitigating bacterial fouling on ship hulls could improve fuel efficiency and reduce maintenance costs. By providing a controlled platform to dissect the interplay between flow conditions and surface properties, our study highlights the broader potential of microfluidic wrinkled surfaces in microbial control strategies across multiple disciplines.

In addition to their role as anti-adhesive substrates, these microstructured surfaces provide a powerful platform for investigating the fundamental interactions between microbes and surface topography. By tuning the pattern geometry, such surfaces can be designed not only to influence bacterial attachment but also to affect bacterial motility, by altering, for instance, movement behaviors, such as twitching[59] or swarming[60], and even modulating growth rates. Moreover, these patterned surfaces offer a unique opportunity to explore how eukaryotic cells, particularly immune cells, respond to complex topographies[61]. While immune cell behavior is known to be highly sensitive to microenvironmental cues, the role of surface topography in modulating immune responses remains poorly understood. Recent studies suggest that specific topographical features can promote chronic inflammation, yet the underlying mechanisms remain elusive[62]. The buckling-induced fabrication method employed in this study presents a distinct advantage by allowing the controlled evaluation of cellular responses to surface topography without altering the underlying material properties. This approach ensures that observed effects arise purely from topographical influences, making it an invaluable tool for studying microbe-surface and immune cell-

https://doi.org/10.1038/s41467-025-68078-5

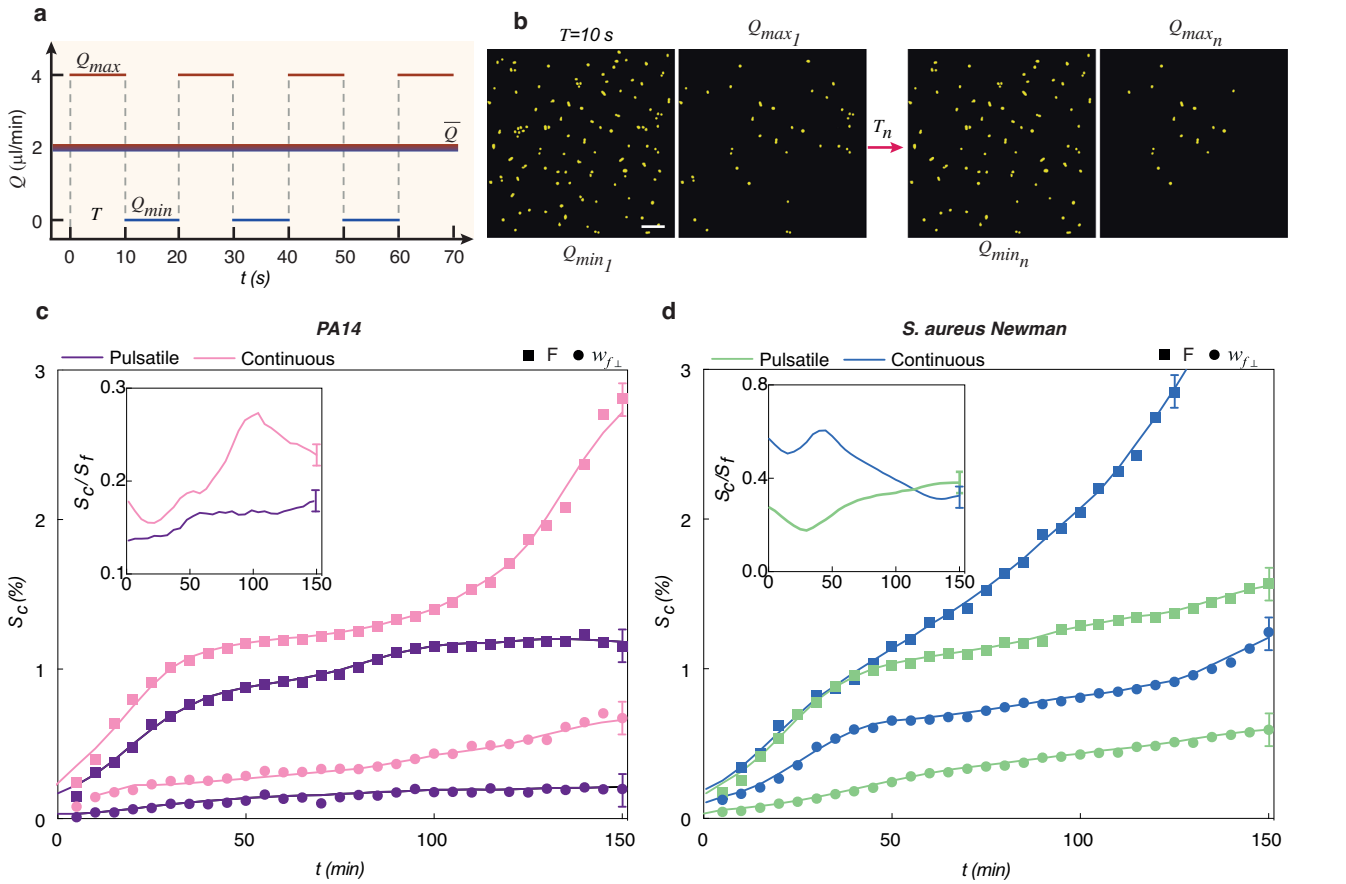

Fig. 8 | Pulsatile flow shapes *Pseudomonas aeruginosa* and *Staphylococcus aureus* attachment on folded surfaces. a Schematic of the pulsatile flow cycle. The syringe pump alternated between $Q_{max} = 4$ µl/min ($\dot{\gamma} = 160\ s^{-1}$) and $Q_{min} = 0$ µl/min with a cycle period of $T = 10$ s. **b** Segmented images of *S. aureus* Newman at different phases of the pulsatile cycle, showing bacterial accumulation at Q_{min} and detachment at Q_{max}. Scale bar, 5 µm. **c** Surface coverage S_c(%) of PA14 under pulsatile (purple) and continuous (pink) flow for flat surfaces (squares) and 5 µm w_f surfaces (circles). Inset: normalized surface coverage (S_c/S_f). **d** Surface coverage S_c(%) of *S. aureus* Newman under pulsatile (green) and continuous (blue) flow for flat surfaces (squares) and 5 µm w_f surfaces (circles). Inset: normalized surface coverage (S_c/S_f). For **c**, **d**, data represent the mean ± SEM from at least $N = 500$ cells per frame, three frames per channel, and three technical channels per condition, with three independent biological replicates.

surface interactions in both fundamental and applied biomedical research.

Overall, this work demonstrates that bacterial adhesion and early colonization are governed not by surface topography or shear alone, but by their combined and dynamic interaction. By introducing controlled wrinkling geometries into microfluidic channels, we revealed bacterial behaviors that cannot be explained by single-factor studies, providing a mechanistic basis for how flow and topography act together. Importantly, our additional experiments under pulsatile flow show that these interactions are also influenced by temporal variations in shear, indicating that time-dependent hydrodynamic cues can further regulate bacterial attachment. Taken together, these results move the field beyond static views of surface effects and point toward design principles that integrate both spatial and temporal control of flow and topography for biofilm management in biomedical, industrial, and environmental settings.

Methods

Patterned surfaces fabrication

Patterned surfaces were fabricated using plasma oxidation of PDMS (PDMS, Sylgard 184 kit, Dow Corning) and Ecoflex (Ecoflex 00-31 Near Clear, Smooth-on). The bilayer structure was generated through uniaxial stretch using a custom-built mechanical actuator, followed by plasma oxidation of a PDMS or Ecoflex substrate. Upon release of the applied strain beyond a critical threshold ϵ_c, a sinusoidal buckling instability was induced, characterized by a wavelength λ and amplitude A, as described by

$$\epsilon_c = \frac{1}{4}\left(\frac{3\bar{E}_s}{\bar{E}_f}\right)^{\frac{2}{3}} \quad (1)$$

$$\lambda = 2\pi h\left(\frac{\bar{E}_f}{3\bar{E}_s}\right)^{\frac{1}{3}} \quad (2)$$

$$A = h\left(\frac{\epsilon}{\epsilon_c} - 1\right)^{\frac{1}{2}} \quad (3)$$

where h is the thickness of the oxidized stiff skin, while $\bar{E}_f$ and $\bar{E}_s$ represent the plane strain modulus and the substrate modulus, respectively. λ is defined as the peak-to-peak distance of the sinusoidal profile, and A as the half of the profile height. By adjusting the applied strain and the plasma treatment parameters (exposure time and power), different geometries can be fabricated. Specifically, 0.5 µm w_s sinusoidal surfaces were obtained by stretching a 2 mm-thick PDMS coupon at $\epsilon = 20\%$ and plasma treating it for 30 min in a MHz plasma chamber (Harrick). The 2 µm w_s sinusoidal surfaces were fabricated using the same strain conditions but with a 5-min exposure in a kHz plasma chamber (Diener Femto). The 5 µm w_f surfaces were produced

https://doi.org/10.1038/s41467-025-68078-5

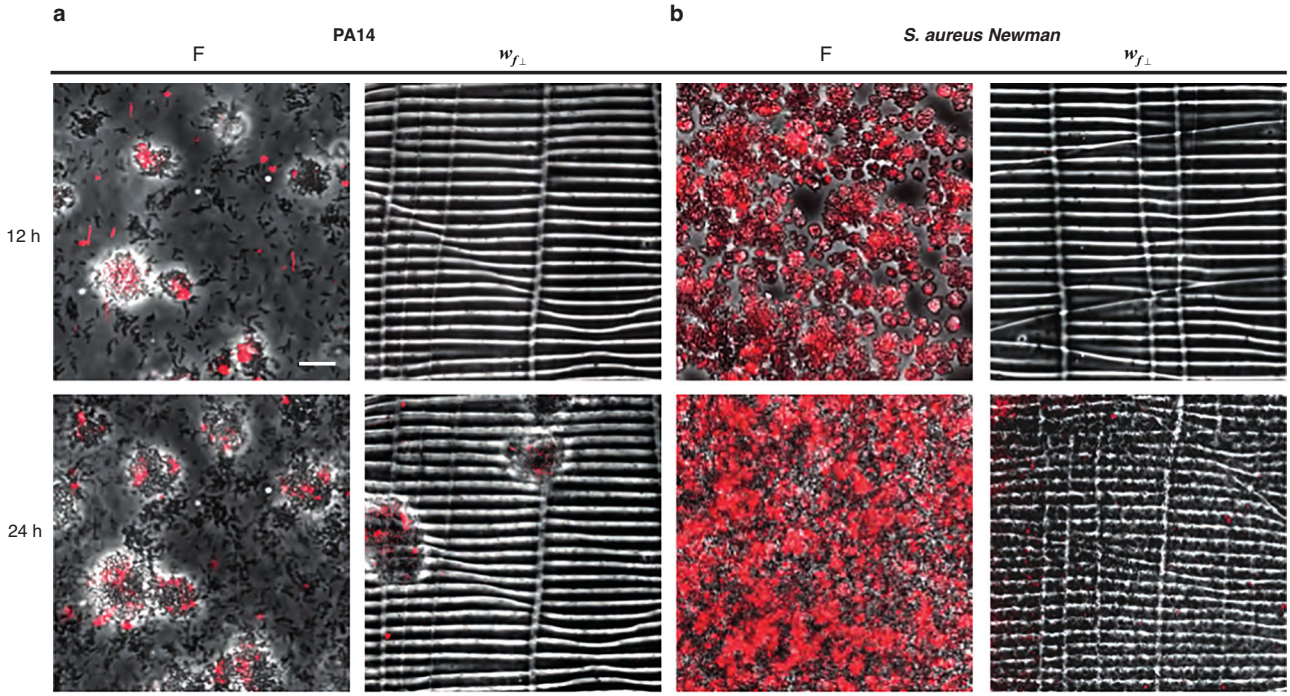

Fig. 9 | Folded surface topography suppresses biofilm formation under high shear. Optical microscopy images showing biofilm formation of **a** *P. aeruginosa* PA14 WT and **b** *S. aureus* Newman on flat (F, first and third column) and 5 µm $w_{f\perp}$ surfaces (second and fourth column) under a shear rate of 200 s^{-1} at 12 h (first line) and 24 h (second line). Biofilm development was tracked by adding propidium iodide (PI, red signal) to the bacterial suspension, which binds extracellular DNA produced by bacteria during micro-colony formation. Scale bar, 10 µm.

by stretching a 2 mm-thick Ecoflex coupon to 80% strain and exposing it to plasma oxidation for 2 min in the MHz plasma chamber. Twenty-micrometer w_f surfaces were obtained by stretching a 2 mm-thick Ecoflex coupon to 50% strain and applying 15 min of plasma oxidation in the MHz plasma chamber. Pattern characterization was carried out using phase-contrast optical microscopy, SEM, and AFM. Wavelengths in the range of 2–20 µm were measured by phase-contrast optical microscopy at ×40 and ×60 magnification and confirmed by AFM. For each sample, at least 20 measurements were collected across different regions and averaged. AFM was further used to obtain full topographical maps, enabling precise quantification of pattern amplitude and validation of the optical wavelength measurements. SEM provided large-area visualization of the surface morphology as well as cross-sectional imaging of the patterns.

Microfluidic assays

For all the experiments, we fabricated a microfluidic chip consisting of six parallel straight channels (Fig. 1a) in PDMS, molded from a silicon master wafer. The chip was assembled by plasma bonding the flat and wrinkled surfaces to the PDMS channels. A syringe pump (Harvard apparatus) was used to perfuse the channels, allowing simultaneous experiments at five different shear rates. For each experiment, syringes were loaded with fresh tryptone broth (TB) or Columbia broth (CB), depending on the bacterial strain. Syringe volumes ranged from 1 to 5 mL, depending on the flow rate. The bacterial inoculum was prepared by measuring the OD at 600 nm (OD_{600}) and adjusting it to the desired concentration, optimized from previous calibration experiments in microfluidic channels. Specifically, an inoculum of $OD_{600} = 0.2$ (~10^8 cells) was used for colonization experiments, while $OD_{600} = 0.005$ was used for biofilm formation assays.

Bacterial cultures

The bacterial strains used in this study were *P. aeruginosa* wild-type (PA14 WT), the motility-deficient mutant PA14Δ*motABCD* (O'Toole strain 2128, 2127), the pili-deficient mutant PA14Δ*pilB* (Kolter collection number ZK3351), and *S. aureus* Newman strain tagged with GFP (NCTC 10833). Bacterial suspensions were prepared by inoculating colonies from agar plates into 3 mL of Terrific Broth (TB, 14 g L^{-1} tryptone) for *P. aeruginosa* strains and Columbia broth (CB, BD DIFCO, 30 g L^{-1}) for *S. aureus*. Cultures were incubated at 37 °C for 4 h. Following incubation, suspensions were diluted with fresh medium to the desired concentration. Fluorescent labeling of PA14 WT was performed using a CellTracker™ Green (Thermo Fisher Scientific) at a final concentration of 3 mM. Cells were incubated at room temperature for 15 min, centrifuged at 2683 RCF to remove the excess dye, and resuspended in fresh medium to the final concentration.

Image acquisition and analysis

Bacterial spatial distribution under flow was analyzed using fluorescence and phase-contrast microscopy (×20 and ×40 magnification) on an inverted microscope (Leica DMi8, LAS X 3.10.0.28982, MetaMorph 7.10.1.161) equipped with an automated stage and temperature-controlled incubator. Images were acquired every 5 min in three different regions of the microfluidic channels, with at least three replicate experiments. Image processing and segmentation were performed using Fiji (ImageJ 1.54p[63]) and Ilastik (Ilastik 1.4.0.post1), a machine learning-based segmentation toolkit[64]. High-resolution imaging of bacterial cells was conducted using AFM (AFM, Nanowizard IV XP, JPK Instruments, Germany) in tapping mode under ambient conditions. Scans were performed over a 50 µm by 50 µm region at 0.5 Hz. Bacterial orientation analysis was performed by dividing fluorescence microscopy images into grids and applying a local fast FFT to each subimage/tile separately. The individual FFTs were then averaged to obtain the angular probability density function (PDF) of bacterial alignment relative to the flow direction. Statistical analyses were performed on datasets comprising at least $N = 500$ individual cells per frame. For each experimental condition, three frames were acquired per microfluidic channel, and three independent channels were

analyzed as technical replicates. Each experiment was repeated on three separate days to provide biological replicates.

Sample preparation for SEM imaging

Bacterial fixation was performed by flowing a 4% PFA solution through the microfluidic channels, followed by a 15-min incubation at room temperature. After fixation, channels were flushed with deionized (DI) water and dried. For imaging, circular patches of PDMS and Ecoflex were obtained using a 8 mm biopsy punch. These discs were mounted on standard SEM stubs (Zeiss, 12.5 mm diameter) using carbon conductive tape (PELCO/Ted Pella). In some cases, samples were cut into thinner strips using a razor blade and mounted on SEM stubs with conductive carbon tape. To ensure stable attachment and improve electrical grounding, a small drop of conductive silver paint (L200N, Agar Scientific) was applied. A thin conductive chromium layer was sputter-coated onto the samples using a Quorum Q150T ES Plus sputter coater equipped with a 57 mm Cr target (Quorum Technologies). Sputtering parameters were set to 120 mA for 20 s, with a tooling factor of 2.30. Samples with bacteria underwent the same metallization procedure following PFA fixation.

FIB-SEM imaging and milling

Samples were imaged using a Zeiss Crossbeam 550 FIB-SEM microscope (Carl Zeiss AG, Jena, Germany). SEM imaging was performed at an accelerating voltage of 5 kV using the secondary electron detector. The working distance was set to 5.1 mm, corresponding to the eucentric height of the FIB beam. To maximize contrast, images were acquired in line averaging mode, with each line sampled 10 times. The scan speed was set to 5, resulting in an acquisition time of approximately 3.5 min per image at a resolution of 4096 × 3072 pixels. Overview images were taken at magnifications of 65 × (pixel spacing: 429.4 nm) and 250 × (pixel spacing: 116.5 nm). Higher-magnification images were acquired using dedicated magnification depending on the wavelength of the pattern. Gallium ion FIB milling was performed at 30 kV in bidirectional scanning mode using SmartFIB, with cycle mode set to loop. The milling current was empirically determined to achieve a clean cut without damaging the sample. The track and pixel spacing were set to 50%, and the ion dose was maintained at 200 $mCcm^{-2}$. Tilt compensation was applied during image acquisition to ensure accurate measurement of the ridge depths.

CFD simulations

We characterized the flow field inside the microchannels with wrinkled walls at different wavelengths and geometries by performing 3D numerical simulations with COMSOL Multiphysics 6.0 (COMSOL AB, Stockholm, Sweden). The hydrodynamic problem was solved using the Laminar Flow interface of the CFD module, implementing the incompressible form of the Navier-Stokes and continuity equations. To optimize computational efficiency, we set a vertical symmetry plane at the centerline of the channel and solved the equations for only one-half of the geometry. By exploiting the periodicity of the patterned surfaces, we applied periodic boundary conditions and simulated only a short portion of the channel in the direction of flow, assigning the inlet and outlet as source and destination surfaces, respectively. The pressure difference $\Delta p = p_{src} - p_{dst}$ between source and destination surfaces was set to match the experimental average velocity U inside the channel. Δp was calculated during the simulations as the pressure value satisfying the additional global equation $U - u_{in}^{av} = 0$, where $u_{in}^{av} = 0$ is the average velocity value of the numerical solution at the inlet. For patterns perpendicular to the flow direction, we used a periodic box with length $L = 10\lambda$ in the direction of flow. For patterns aligned to the direction of flow, we set $L = \lambda$. In both configurations, the mesh was swept along the pattern direction and consisted of approximately 1.5×10^5 elements. To analyze the flow field near surface-attached bacterial cells, we incorporated 3D objects representing individual bacteria within the simulated microchannel. Each bacterium was modeled as a cylinder with hemispherical caps, with radius $R = 0.5$ µm and a total length $L = 3$ µm. Simulations were performed with single cells in three different positions on the wrinkled walls: in a minimum, in a maximum, and in an intermediate position. In the intermediate position, the cell is touching the surface at a distance $\lambda/4$ from a maximum. To avoid artifacts due to symmetry constraints, we modeled cells across the symmetry plane whenever possible, ensuring that only half of the bacterium was explicitly simulated while the other half was mirrored. When this was not feasible, we placed cells sufficiently far from the symmetry plane to minimize flow perturbations caused by their mirrored images. A finer mesh was used around the bacterial cells to improve accuracy, leading to a total of approximately 5×10^6 elements.

Reporting summary

Further information on research design is available in the Nature Portfolio Reporting Summary linked to this article.

Data availability

Additional data supporting this study are available in the Supplementary Information. A Source data file containing all data displayed in the figures and reported in the tables is provided with this paper and is accessible at https://doi.org/10.5281/zenodo.17303681. Any remaining data underlying this study are available from the corresponding author upon request. Source data are provided with this paper.

References

1. Krajewski, S. et al. Bacterial interactions with proteins and cells relevant to the development of life-threatening endocarditis studied by use of a quartz-crystal microbalance. *Anal. Bioanal. Chem.* **406**, 3395–3406 (2014).
2. Cheng, Y., Feng, G. & Moraru, C. I. Micro-and nanotopography sensitive bacterial attachment mechanisms: a review. *Front. Microbiol.* **10**, 191 (2019).
3. Caldara, M., Belgiovine, C., Secchi, E. & Rusconi, R. Environmental, microbiological, and immunological features of bacterial biofilms associated with implanted medical devices. *Clin. Microbiol. Rev.* **35**, e00221–20 (2022).
4. Hsu, L. C., Fang, J., Borca-Tasciuc, D. A., Worobo, R. W. & Moraru, C. I. Effect of micro-and nanoscale topography on the adhesion of bacterial cells to solid surfaces. *Appl. Environ. Microbiol.* **79**, 2703–2712 (2013).
5. Tripathy, A., Sen, P., Su, B. & Briscoe, W. H. Natural and bioinspired nanostructured bactericidal surfaces. *Adv. Colloid Interface Sci.* **248**, 85–104 (2017).
6. Skoog, S. A., Kumar, G., Narayan, R. J. & Goering, P. L. Biological responses to immobilized microscale and nanoscale surface topographies. *Pharmacol. Ther.* **182**, 33–55 (2018).
7. Luan, Y. et al. Bacterial interactions with nanostructured surfaces. *Curr. Opinion Colloid Interface Sci.* **38**, 170–189 (2018).
8. Lee, S. W., Phillips, K. S., Gu, H., Kazemzadeh-Narbat, M. & Ren, D. How microbes read the map: effects of implant topography on bacterial adhesion and biofilm formation. *Biomaterials* **268**, 120595 (2020).
9. Ivanova, E. P. et al. Impact of nanoscale roughness of titanium thin film surfaces on bacterial retention. *Langmuir* **26**, 1973–1982 (2010).
10. Mainwaring, D. E. et al. The nature of inherent bactericidal activity: insights from the nanotopology of three species of dragonfly. *Nanoscale* **8**, 6527–6534 (2016).
11. Elbourne, A., Crawford, R. J. & Ivanova, E. P. Nano-structured antimicrobial surfaces: from nature to synthetic analogues. *J. Colloid Interface Sci.* **508**, 603–616 (2017).
12. Tuson, H. H. & Weibel, D. B. Bacteria–surface interactions. *Soft Matter* **9**, 4368–4380 (2013).

13. Vasudevan, R., Kennedy, A. J., Merritt, M., Crocker, F. H. & Baney, R. H. Microscale patterned surfaces reduce bacterial fouling-microscopic and theoretical analysis. *Colloids Surf. B Biointerfaces* **117**, 225–232 (2014).
14. Hong, S.-H. et al. Surface waves control bacterial attachment and formation of biofilms in thin layers. *Sci. Adv.* **6**, eaaz9386 (2020).
15. Pellegrino, L., Kriem, L. S., Robles, E. S. & Cabral, J. T. Microbial response to micrometer-scale multiaxial wrinkled surfaces. *ACS Appl. Mater. Interfaces* **14**, 31463–31473 (2022).
16. Hizal, F. et al. Impact of 3D hierarchical nanostructures on the antibacterial efficacy of a bacteria-triggered self-defensive antibiotic coating. *ACS Appl. Mater. Interfaces* **7**, 20304–20313 (2015).
17. Chang, Y.-R., Weeks, E. R. & Ducker, W. A. Surface topography hinders bacterial surface motility. *ACS Appl. Mater. Interfaces* **10**, 9225–9234 (2018).
18. Mok, R., Dunkel, J. & Kantsler, V. Geometric control of bacterial surface accumulation. *Phys. Rev. E* **99**, 052607 (2019).
19. Zheng, S. et al. Implication of surface properties, bacterial motility, and hydrodynamic conditions on bacterial surface sensing and their initial adhesion. *Front. Bioeng. Biotechnol.* **9**, 643722 (2021).
20. Surapaneni, V. A. et al. Groovy and gnarly: surface wrinkles as a multifunctional motif for terrestrial and marine environments. *Integr. Comp. Biol.* **62**, 749–761 (2022).
21. Demenego, G. et al. Neurodevelopmental origins of structural and psychomotor defects in CXCR4-linked primary immunodeficiency. *Neuron* **113**, 2636–2655 (2025).
22. Rusconi, R., Guasto, J. S. & Stocker, R. Bacterial transport suppressed by fluid shear. *Nat. Phys.* **10**, 212–217 (2014).
23. Secchi, E. et al. The effect of flow on swimming bacteria controls the initial colonization of curved surfaces. *Nat. Commun.* **11**, 2851 (2020).
24. Lee, Y. K., Won, Y.-J., Yoo, J. H., Ahn, K. H. & Lee, C.-H. Flow analysis and fouling on the patterned membrane surface. *J. Membr. Sci.* **427**, 320–325 (2013).
25. Wang, Q. & Zhao, X. A three-dimensional phase diagram of growth-induced surface instabilities. *Sci. Rep.* **5**, 8887 (2015).
26. Allen, J. The classification of cross-stratified units. with notes on their origin. *Sedimentology* **2**, 93–114 (1963).
27. Efimenko, K. et al. Nested self-similar wrinkling patterns in skins. *Nat. Mater.* **4**, 293–297 (2005).
28. Genzer, J. & Groenewold, J. Soft matter with hard skin: from skin wrinkles to templating and material characterization. *Soft Matter* **2**, 310–323 (2006).
29. Bayley, F. A., Liao, J. L., Stavrinou, P. N., Chiche, A. & Cabral, J. T. Wavefront kinetics of plasma oxidation of polydimethylsiloxane: limits for sub-μm wrinkling. *Soft Matter* **10**, 1155–1166 (2014).
30. Nania, M., Foglia, F., Matar, O. K. & Cabral, J. T. Sub-100 nm wrinkling of polydimethylsiloxane by double frontal oxidation. *Nanoscale* **9**, 2030–2037 (2017).
31. Pellegrino, L., Khodaparast, S. & Cabral, J. T. Orthogonal wave superposition of wrinkled, plasma-oxidised, polydimethylsiloxane surfaces. *Soft Matter* **16**, 595–603 (2020).
32. Pellegrino, L., Tan, A. & Cabral, J. T. Ripple patterns spontaneously emerge through sequential wrinkling interference in polymer bilayers. *Phys. Rev. Lett.* **128**, 058001 (2022).
33. Nakazawa, K. et al. A human septin octamer complex sensitive to membrane curvature drives membrane deformation with a specific mesh-like organization. *J. Cell Sci.* **136**, jcs260813 (2023).
34. Li, B., Cao, Y.-P., Feng, X.-Q. & Gao, H. Mechanics of morphological instabilities and surface wrinkling in soft materials: a review. *Soft Matter* **8**, 5728–5745 (2012).
35. Stroock, A. D. et al. Chaotic mixer for microchannels. *Science* **295**, 647–651 (2002).
36. Pyke, K. E., Dwyer, E. M. & Tschakovsky, M. E. Impact of controlling shear rate on flow-mediated dilation responses in the brachial artery of humans. *J. Appl. Physiol.* **97**, 499–508 (2004).
37. Zöttl, A. et al. Dynamics of individual Brownian rods in a microchannel flow. *Soft Matter* **15**, 5810–5814 (2019).
38. Shen, Y., Siryaporn, A., Lecuyer, S., Gitai, Z. & Stone, H. A. Flow directs surface-attached bacteria to twitch upstream. *Biophys. J.* **103**, 146–151 (2012).
39. Leighton, T. L., Buensuceso, R. N., Howell, P. L. & Burrows, L. L. Biogenesis of Pseudomonas aeruginosa type IV pili and regulation of their function. *Environ. Microbiol.* **17**, 4148–4163 (2015).
40. Duvernoy, M.-C. et al. Asymmetric adhesion of rod-shaped bacteria controls microcolony morphogenesis. *Nat. Commun.* **9**, 1120 (2018).
41. Roberge, N. A. & Burrows, L. L. Building permits-control of type IV pilus assembly by pilB and its cofactors. *J. Bacteriol.* **206**, e00359–24 (2024).
42. Lecuyer, S. et al. Shear stress increases the residence time of adhesion of Pseudomonas aeruginosa. *Biophys. J.* **100**, 341–350 (2011).
43. Parente, R. et al. A multilayered imaging and microfluidics approach for evaluating the effect of fibrinolysis in Staphylococcus aureus biofilm formation. *Pathogens* **12**, 1141 (2023).
44. Baba, T., Bae, T., Schneewind, O., Takeuchi, F. & Hiramatsu, K. Genome sequence of Staphylococcus aureus strain Newman and comparative analysis of staphylococcal genomes: polymorphism and evolution of two major pathogenicity islands. *J. Bacteriol.* **190**, 300–310 (2008).
45. Forson, A. M., van der Mei, H. C. & Sjollema, J. Impact of solid surface hydrophobicity and micrococcal nuclease production on Staphylococcus aureus newman biofilms. *Sci. Rep.* **10**, 12093 (2020).
46. Parsons, J. B., Westgeest, A. C., Conlon, B. P. & Fowler Jr, V. G. Persistent methicillin-resistant Staphylococcus aureus bacteremia: host, pathogen, and treatment. *Antibiotics* **12**, 455 (2023).
47. Liesenborghs, L., Verhamme, P. & Vanassche, T. Staphylococcus aureus, master manipulator of the human hemostatic system. *J. Thromb. Haemost.* **16**, 441–454 (2018).
48. McAdow, M. et al. Preventing Staphylococcus aureus sepsis through the inhibition of its agglutination in blood. *PLoS Pathog.* **7**, e1002307 (2011).
49. Belgiovine, C. et al. Interaction of bacteria, immune cells, and surface topography in periprosthetic joint infections. *Int. J. Mol. Sci.* **24**, 9028 (2023).
50. Gammie, A. et al. International continence society guidelines on urodynamic equipment performance. *Neurourol. Urodyn.* **33**, 370–379 (2014).
51. Secchi, E. et al. The structural role of bacterial eDNA in the formation of biofilm streamers. *Proc. Natl. Acad. Sci. USA* **119**, e2113723119 (2022).
52. Savorana, G., Słomka, J., Stocker, R., Rusconi, R. & Secchi, E. A microfluidic platform for characterizing the structure and rheology of biofilm streamers. *Soft Matter* **18**, 3878 - 3890 (2022).
53. Lee, S. W., Phillips, K. S., Gu, H., Kazemzadeh-Narbat, M. & Ren, D. How microbes read the map: effects of implant topography on bacterial adhesion and biofilm formation. *Biomaterials* **268**, 120595 (2021).
54. Nicolle, L. E. Catheter associated urinary tract infections. *Antimicrob. Resist. Infect. Control* **3**, 1–8 (2014).
55. Werneburg, G. T. Catheter-associated urinary tract infections: current challenges and future prospects. *Res. Rep. Urol.* **14**, 109–133 (2022).
56. Marschall, J., Carpenter, C. R., Fowler, S. & Trautner, B. W. Antibiotic prophylaxis for urinary tract infections after removal of urinary catheter: meta-analysis. *Bmj* **346**, f3147 (2013).

57. Holmes, A. H. et al. Understanding the mechanisms and drivers of antimicrobial resistance. *Lancet* **387**, 176–187 (2016).
58. Dean, B. & Bhushan, B. Shark-skin surfaces for fluid-drag reduction in turbulent flow: a review. *Philos. Trans. R. Soc. A Math. Phys. Eng. Sci.* **368**, 4775 - 4806 (2010).
59. Gomez, S. et al. Substrate stiffness impacts early biofilm formation by modulating Pseudomonas aeruginosa twitching motility. *eLife* **12**, e81112 (2023).
60. Ariel, G. et al. Swarming bacteria migrate by Lévy Walk. *Nat. Commun.* **6**, 8396 (2015).
61. Lauta, F. C., Pellegrino, L. & Rusconi, R. Macrophages on the wrinkle: exploring microscale interactions with substrate topography. *Biophys. Rev.* **5**, 022001 (2024).
62. Vinci, V. et al. Breast implant surface topography triggers a chronic-like inflammatory response. *Life Sci. Alliance* **7**, e202302132 (2024).
63. Schneider, C. A., Rasband, W. S. & Eliceiri, K. W. NIH image to ImageJ: 25 years of image analysis. *Nat. Methods* **9**, 671–675 (2012).
64. Berg, S. et al. ilastik: interactive machine learning for (bio)image analysis. *Nat. Methods* **16**, 1226–1232 (2019).

Acknowledgements

This work was supported by EU funding within the Italian Ministry of University and Research (MUR) PNRR Extended Partnership initiative on Emerging Infectious Diseases (project no. PE00000007, INF-ACT) to R.R., EU HORIZON-TMA-MSCA-PF-EF investigating microbial colonization and removal on dynamic patterned surfaces (grant no. 101110029, MOBILE) to L.P., and by a grant from the Italian Ministry of University and Research (MUR), Dipartimenti di Eccellenza 2023-2027 (I.232/2016, art. 1, commi 314-337) to V.C., R.C., and F.M.. E.D.I. and M.C. are grateful to Humanitas University Office of Information Technology for the computing resources maintenance. L.P., V.C., R.C., and F.M. gratefully acknowledge the support of the ISIS@MACH ITALIA Research Infrastructure, the hub of ISIS Neutron and Muon Source (UK), [MUR official registry U. 0008642.28-05-2020-16th April 2020]. IM@IT is listed in the Italian Ministry of University and Research's Piano Nazionale delle Infrastrutture di Ricerca (PNIR 2021–2027) "in the broader notion of ISIS", and ISIS Facility and IM@IT are jointly listed in high-priority RI's (see Table 6, page 30, note 38, PNIR in 2021–2027).

Author contributions

L.P. and R.R. conceived and designed the project. L.P. conducted the microfluidic experiments and performed data analysis. L.P., G.S., and E.S. carried out numerical simulations and interpreted the results. L.P., V.C., R.C., and F.M. performed and analyzed AFM measurements. M.C. and E.D.I. conducted and analyzed SEM measurements. S.L. and C.B. contributed to data analysis and interpretation. V.V., M.K., and R.R. acquired funding and supervised the research. L.P. and R.R. wrote the original draft, and all authors contributed to reviewing and editing the manuscript.

Competing interests

The authors declare no competing interests.

Additional information

Supplementary information The online version contains supplementary material available at https://doi.org/10.1038/s41467-025-68078-5.

Correspondence and requests for materials should be addressed to Luca Pellegrino or Roberto Rusconi.

Peer review information *Nature Communications* thanks James Henderson and the other anonymous reviewers for their contribution to the peer review of this work. A peer review file is available.